LLNL-BOOK-692701

Chapter 1

Dispersed Interferometers

David J. Erskine

Lawrence Livermore National Laboratory,
7000 East Ave, Livermore, CA 94550, USA,
erskine1@llnl.gov

We describe dispersed interferometers, including dispersed Fourier Transform spectroscopy (dFTS), externally dispersed interferometer (EDI) also known as dispersed fixed delay interferometer (DFDI), spatial heterodyning spectroscopy (SHS) and the similar heterodyned holographic spectroscopy (HHS).

1. Overview

Spectroscopy via dispersed interferometry is a hybrid between two well established techniques of pure interferometry (such as Fourier Transform Spectroscopy) and dispersive spectroscopy using a prism or grating. Figure 1 is a notional diagram of various spectrograph techniques, displayed in Fourier space, with purely dispersive and purely interferometric at the top and bottoms, and the hybrids in between. The horizontal axis is the spatial frequency along the dispersion axis, or features per wavenumber. (It is convenient to use wavenumber ($\sigma = 1/\lambda$) instead of wavelength λ for dispersion in interferometry.) Since the unit of σ is cm^{-1}, this frequency has units of delay or cm. The horizontal axis can be considered the distribution of optical pathlengths needed to create the resolution. Imagine these pathlength differences, for example, between the different grooves of a diffraction grating, or between two arms of an interferometer.

In the top panel (a), a high resolution spectrograph having narrow instrument response peak in wavenumber space requires a wide peak in delay or Fourier space. From the uncertainty principle, the product of the full width half max (FWHM) peak widths in frequency and wavenumber spaces is about 0.88. The resolution is $R = \sigma/\Delta\sigma$; hence $R = 2\rho_{hwhm}\sigma/0.88$, where ρ_{hwhm} is the Gaussian half width at half height, because we are only plotting the positive frequencies for convenience.

The high resolution peak is depicted as having a smaller height than the lower resolution peak to suggest that as we reduce the slit width to achieve higher resolution in a classical dispersive spectrograph, the amount of light from an extended source passing through the narrower slits decreases. (This would not apply to a

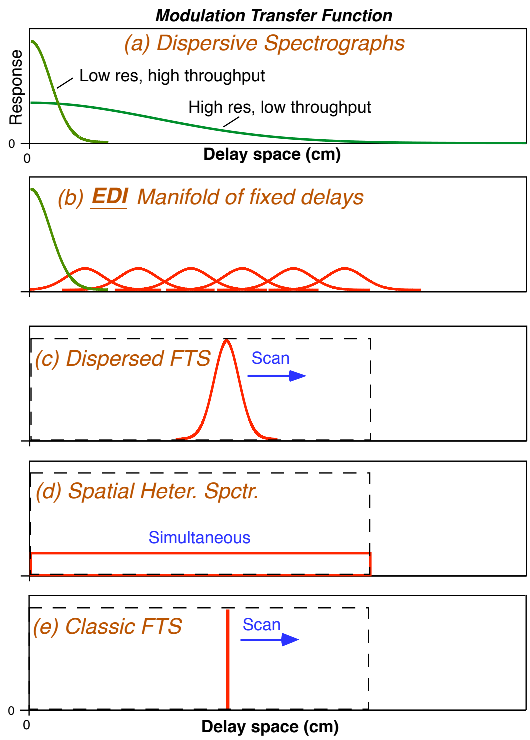

Fig. 1. Notional arrangement of astronomical spectrograph systems, from purely dispersive (a) to purely interferometric (e), in Fourier space (features per wavenumber, or delay space). For all methods one needs to cover maximal delay space to achieve high resolution. (b) The Externally Dispersed Interferometer (EDI) measures delay space in chunks (single or multiple peaks at user chosen positions) on an integrating detector; (c) dispersed Fourier Transform Spectroscopy (FTS) scans delay space with a single medium-wide peak using a time-responsive detector. (d) Spatial Heterodyning Spectroscopy (SHS) splays a range of delays spatially along a detector, recording at once the interferogram on an integrating detector; (e) purely interferometric FTS maps out delay space directly with a narrow peak, measuring the interferogram. Graphic reproduced from Ref. 1. (See electronic edition for a color version of this figure.)

diffraction-limited source from an adaptive optics-corrected telescope).

2. Dispersed Fourier Transform Spectrometer (dFTS)

2.1. *Classic undispersed FTS*

The bottom panel (e) of Fig. 1 depicts behavior of the classic undispersed interferometer or Fourier Transform Spectrometer (FTS). The delay is sampled by a narrow peak and scanned contiguously *vs.* time over the wide delay range needed to record high resolution information. The peak is very narrow because there is no disperser or bandpass filter, so the essentially single-pixel detector responds to a wide wavenumber range — the peak width is the reciprocal of the wide bandwidth.

Scanning over the delay range measures the interferogram of the spectrum. A Fourier transform is then applied to convert the interferogram into a spectrum. It only takes about a couple of cm of delay range to develop, say, 50,000 resolution at 0.5 μm wavelength. So interferometers do not need to be very large to achieve high resolution.

The FTS has the advantage over conventional dispersive spectrographs of being very compact, with an output lineshape that is very robust to changes in the input beam pupil. (All dispersed interferometers tend to share this robustness). Disadvantages include the inability to measure time-dependent or pulsed phenomenon, because of the time needed to scan over the delay. Furthermore, its detector must record a high frequency time-dependent signal (as it scans over fringes), so it cannot use time-integrating detectors optimized for sensitivity.

Because fringes from all the wavenumbers combine on a single pixel, the net fringe signal for the classic FTS is washed out (diminished by the square root of the number of independent wavenumbers being measured), so the photon signal to noise ratio is usually too poor for many astronomical sources. However, in the infrared there are many more photons per unit of power, so the FTS has found useful remote sensing applications in long wavelengths, especially since its compactness makes

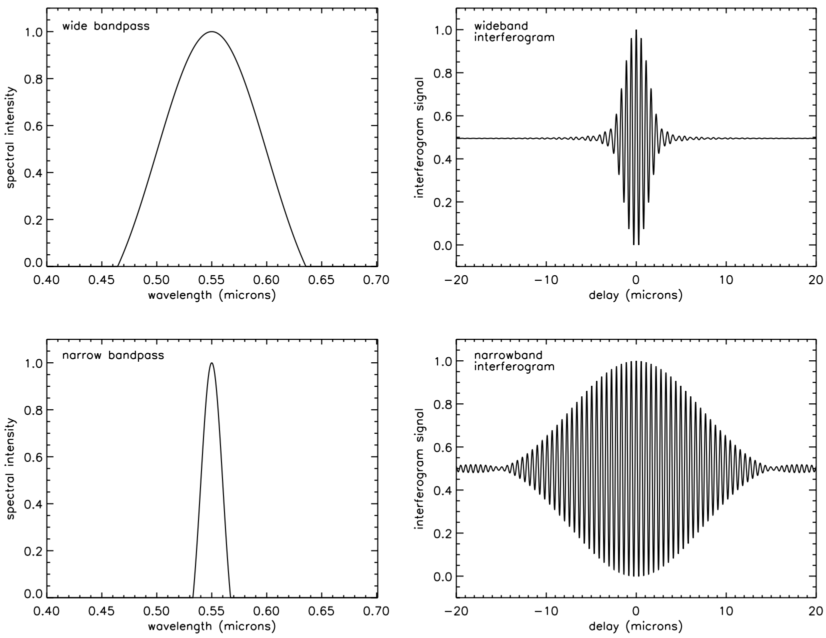

Fig. 2. When the bandwidth is narrowed by insertion of a filter or use of an external disperser, the interferogram fringe pattern becomes reciprocally wider in delay space. Simulated interferograms as shown. Graphics reprinted from Ref. 2, Copyright (2007), with permission from AAS.

airborne and spaceborne platforms practical. In comparison, an infrared dispersive spectrograph of comparable resolution could be prohibitively large because its size scales with the long wavelength.

2.2. *Adding dispersion to increase fringe visibility*

A dispersed FTS (dFTS) is created by adding a disperser in series with the interferometer,[2–4] depicted as Fig. 1(c). Figure 2 shows how decreasing the bandwidth, by insertion of a filter or a dispersive element in series with the FTS, reciprocally increases the width of the interferogram in delay space (hence the wider peak in Fig. 1[c] compared with Fig. 1[e]). This increases the fringe visibility, and hence photon signal to noise ratio for a given delay, making the dFTS much more practical for astronomical use than the classical (undispersed) FTS.

The disperser organizes the data into narrow bandwidth channels. Each is an independent FTS interferogram similar to an undispersed FTS, but having much greater fringe visibility. A custom "FROID" algorithm was used to assemble the manifold parallel channel information into a single high resolution (R=50,000) broadband spectrum.[2]

A prototype version (2007) of the dFTS[2] was tested on starlight at the Clay Center Observatory at the Dexter-Southfield School in Brookline, Massachusetts, on a 25 inch telescope that regularly achieves 1″ seeing. Figure 3 shows the zero point radial velocity reproducibility from night to night, observing a Th-Ne spectral lamp. The variability ∼10 m/s is believed primarily due to temperature drifts of the instrument, which was not housed in a temperature controlled environment but one with ∼5 °C changes in ambient air temperature.

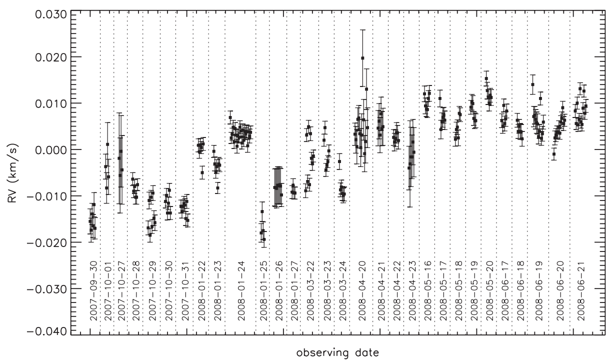

Fig. 3. Zero point radial velocity reproducibility from night to night, observing a Th-Ne spectral lamp. The variability ∼10 m/s is believed primarily due to temperature drifts of the instrument, which was not housed in a temperature controlled environment but one with ∼5 °C changes in ambient air temperature. Graphics reprinted from Ref. 3, Copyright (2009), with permission from AAS.

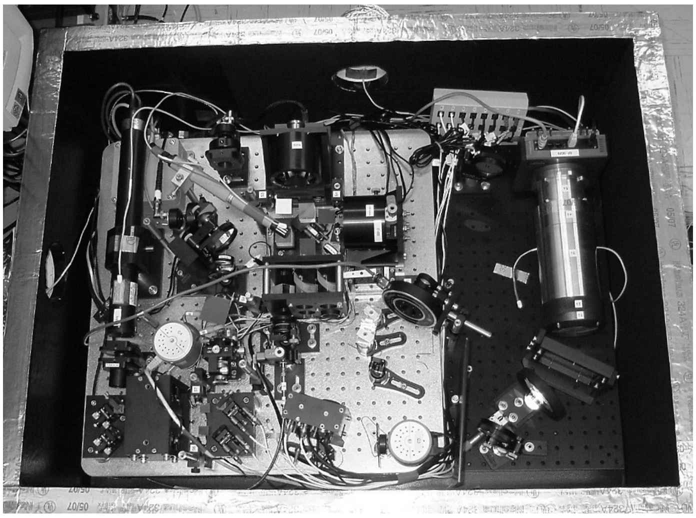

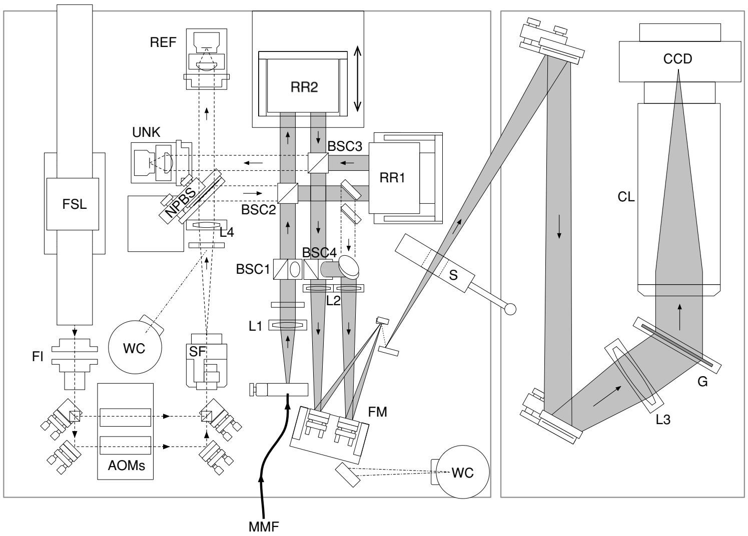

Fig. 4. Photograph and schematic of the second version of the dFTS. The key element distinguishing it from a classic FTS is the use of a dispersive spectrograph (right side) ahead of the detector. Graphics reprinted from Ref. 3, Copyright (2009), with permission from AAS.

The 2nd generation (2009) instrument (Fig. 4) measured[3] single-line spectroscopic binaries at the Steward Observatory 2.3 m Bok Telescope. This apparatus was more compact than the first. Figure 5 shows radial velocities of the F6V star 19 Draconis with a velocity scatter of 27.5 m/s. Measurements on double-lined spectroscopic binaries were also performed there.[4]

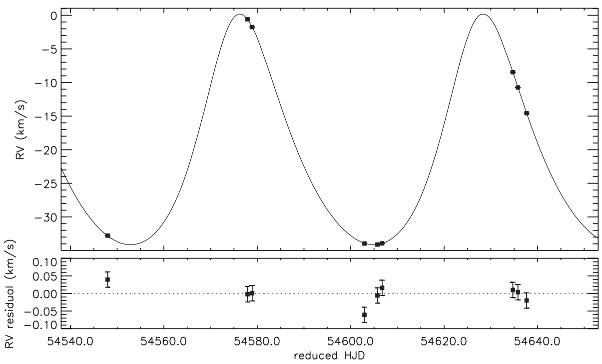

Fig. 5. The radial velocity scatter of this measurement of F6V star 19 Draconis was 27.5 m/s. Graphics reprinted from Ref. 3, Copyright (2009), with permission from AAS.

3. Externally Dispersed Interferometry (EDI)

3.1. *Interferometer in Series with Dispersive Spectrograph*

Externally dispersed interferometry[1,5,7–16] (EDI), also called by others dispersed fixed delay interferometry[11–13] (DFDI), is the series combination of a fixed delay interferometer with a dispersive spectrograph (Figs. 6, 7). The interferometer creates a uniform sinusoidal grid or comb in its transmission function versus wavenumber σ (units of cm^{-1}), as $T(\sigma) = 0.5[1 + \cos(2\pi\sigma\tau)]$, having a frequency along the wavenumber axis proportional to the interferometer delay τ (units of cm). This is typically 1 to 5 cm, depending on the linewidths in the input spectrum (for Doppler), or the resolution desired (increases with τ). It is set by choice of a glass etalon thickness and mirror positions that control pathlength difference between two interferometer arms.

3.1.1. *Moiré Patterns Reveal Doppler and High Resolution Features*

A heterodyning effect caused by multiplication of the periodic transmission $T(\sigma)$ against the stellar input spectrum creates moiré fringe patterns on the detector that sum with the ordinary spectrum. These moiré patterns are high frequencies (narrow features) of the input spectrum beaten down (shifted) to lower frequencies, which can better survive slit blurring and paucity of detector pixels.

This heterodyning creates a new sensitivity peak at a user selectable high frequency (Fig. 10, left), while preserving the native spectrograph sensitivity peak centered at zero frequency. This allows precision radial Doppler velocimetry[7,12,14] and high resolution spectroscopy[1,5,15,16] with a much lower resolution native spectrograph than without the interferometer. Hence EDI imparts a resolution boosting ability, and this occurs over the entire native bandwidth.

The inclusion of the interferometer, by its very uniform spectral fiducial comb,

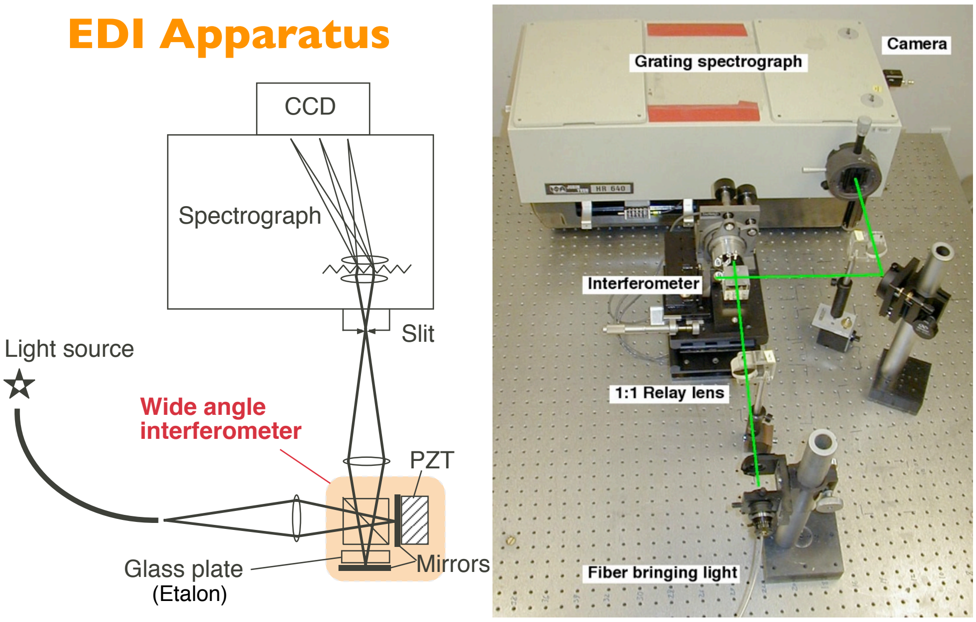

Fig. 6. Schematic (left) and photo (right) of an externally dispersed interferometer assembled from components found in a typical university optics lab and a 20k resolution Jobin-Yvon HR640 grating spectrograph operating near 500 nm. The interferometer delay was 1.1 cm. Together with an iodine cell (not shown), this apparatus measured the 12 m/s amplitude tugging of the Moon on the Earth (Fig. 11) from fringing spectra (Fig. 7[right]) of sunlight fed by fiber from a rooftop heliostat. No environmental thermal or mechanical stabilization was used (the short exposure times did not require interferometer fringe stabilization). Schematic and photograph reproduced from Ref. 5. (See electronic edition for a color version of this figure.)

can also boost the stability to undesired changes in pupil, focal spot or wavelength drifts in the disperser, which often plague a native spectrograph used alone.

3.1.2. *Heterodyning Allows Lower Resolution Native Spectrographs*

By permitting the use of a lower resolution spectrograph, the EDI technique reaps advantages of the wider bandwidth and higher throughput of a lower resolution spectrograph. (For a fixed number of pixels, bandwidth increases approximately reciprocally to native resolving power.) The wider bandwidth uses a larger fraction of the stellar flux, which can improve the photon-limited signal-to-noise ratio. The wider slits and greater tolerance to focal errors of a lower resolution spectrograph allows lenses and gratings to be optimized for high efficiency rather than for a stable focal spot.

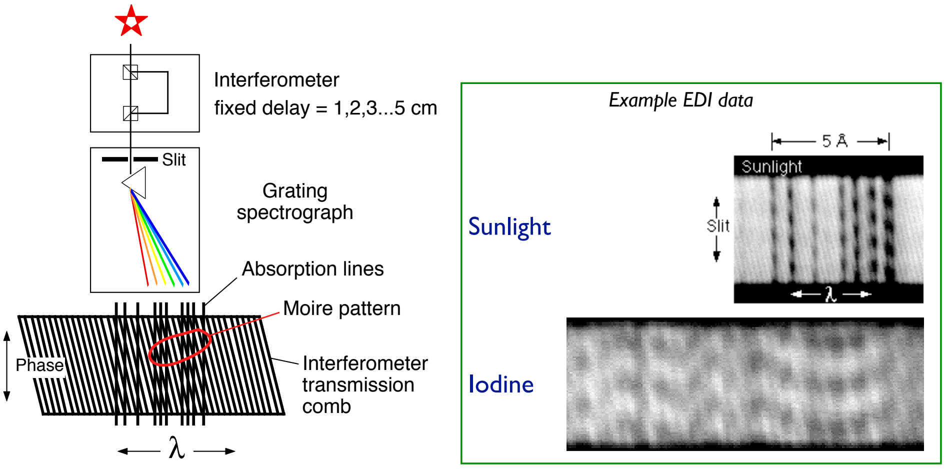

Fig. 7. (Left) Schematic of EDI, which is an interferometer of one or several fixed delay values (1 to 5 cm) in series with a dispersive spectrograph. The interferometer creates a sinusoidal comb with a period $\sim 1/\tau$. The input spectral features combine with the sinusoid to create moiré patterns. Phase shifts are proportional to the Doppler velocity. The shape of the moiré can be processed to recover input spectral features at higher resolution than the native spectrograph alone (10x boost has been demonstrated). The schematic was reproduced from Ref. 6. (Right) Solar and iodine fringing spectra near 508 nm, when measured separately by the EDI.[7] A small portion of total 13 nm bandwidth is shown. Smile-like features in iodine are due to a set of absorption lines whose spacing varies gradually from slightly less than the comb to slightly more. (See electronic edition for a color version of this figure.)

3.1.3. *Phase Stepping Elucidates Moiré Patterns*

Figure 7 (left) shows the notional diagram of EDI and how absorption lines acting against the sinusoidal comb created by the interferometer form moiré fringe patterns. Figure 7 (right) shows measured moiré patterns for sunlight and the iodine spectrum, and Fig. 8(a, b) simulates them for two line pairs of different spacing with (b), and without (a), slit blurring.

Data are usually taken with several exposures while incrementing the interferometer delay in subwavelength amounts, called “phase stepping”. This allows the fringing (moiré) and nonfringing (ordinary spectrum) components to be separated during analysis, since only the true fringes will vary synchronously to the commanded phase dither. Both of these components can provide useful spectral information which can be combined to form the net EDI output, or used separately.

Because the fringing component involves differences between exposures, and only responds to signals synchronous to the applied interferometer dither, the EDI is naturally immune to additive fixed-pattern errors that can plague the ordinary spectrum. Hence, in many cases the EDI can produce a cleaner output spectrum than the native spectrograph, even at the same resolution as the native.

The temporal phase stepping allows use of echelle spectrographs, which may

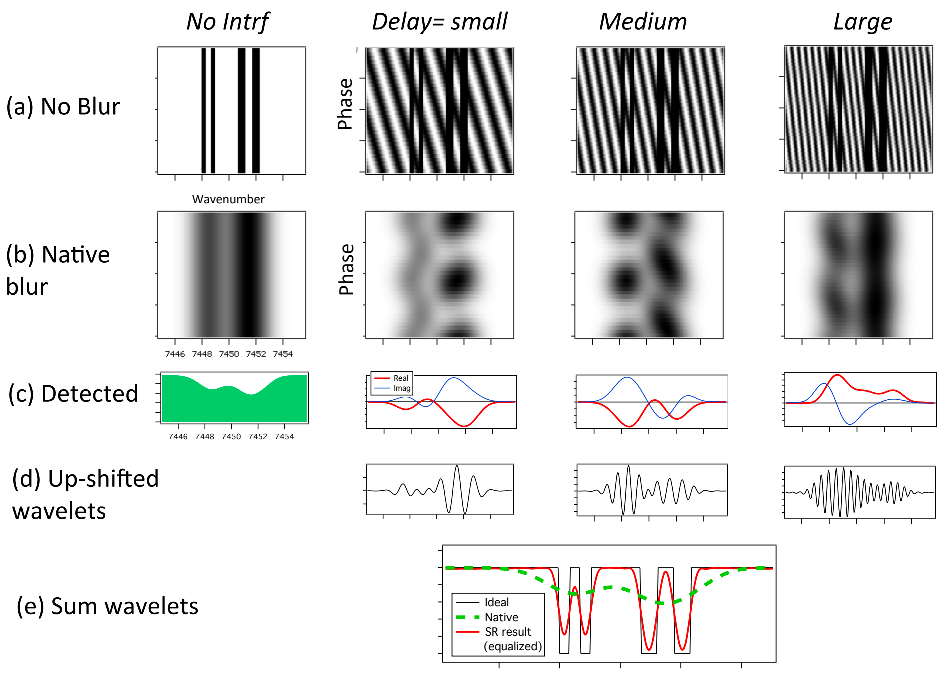

Fig. 8. (a-c) Simulation of heterodyning and moiré formation that occurs optically in the instrument, and then (d, e) its reversal during reconstruction of the resolution-boosted spectrum. Moiré patterns using a test absorption spectrum of two pairs of black lines (black curve in [e]). (a) Sinusoidal comb multiplies input spectrum — comb frequency is proportional to delay τ. Only three delays (0.75, 1.25, 2 cm) of eight shown. (a) Without blur. (b) With blur, the comb is unresolved but moiré pattern remains. (c) Complex expression of moiré (whirl or **W**) from Fig. 9. Red (real), blue (imaginary). (d) Whirls upshifted in frequency; real part taken to form wavelets. (e) Sum of wavelets forms reconstructed output (red curve). An equalization step weights the wavelets to eliminate ringing. Native spectrum (dashed green) has insufficient resolution (2 cm^{-1}) to resolve test pair, but EDI output (red) easily resolves them. Graphs are $\sim$10 cm^{-1} across at average wavenumber of 7450 cm^{-1}. Graphics reproduced from Ref. 1. (See electronic edition for a color version of this figure.)

have a narrow beam as small as 1 pixel high. These are useful because of their wide bandwidth. Alternatively, linear spectrographs having a tall slit can splay the phase spatially along the slit, or apply both spatial and temporal variations.

An interferometer has two complementary phased outputs whose intensities, when summed, equal the input (assuming ideal optics). The complementary output can also be used to produce an EDI signal if it is detected on separate pixels.

3.1.4. *EDI Instrument Lineshape as a Wavelet*

Figure 10 (right) compares the instrument lineshape versus wavenumber between a conventional spectrograph and the EDI. Whereas the conventional lineshape is a peak (b or c), the EDI lineshape is a wavelet (a) which has an envelope set by the

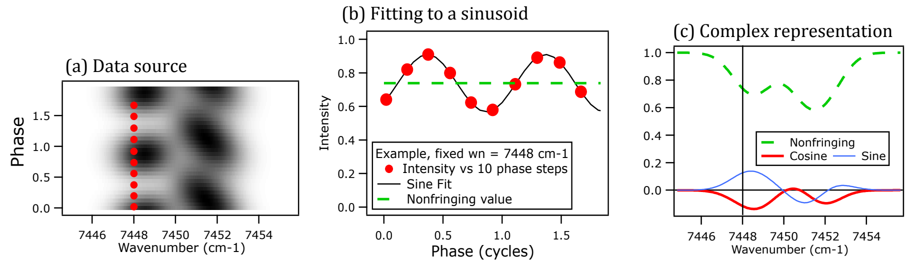

Fig. 9. How to convert a moiré pattern to complex data. (a) Vertical lineout across multiphase stack for a given wavenumber produces an intensity versus phase plot (b), which is fitted to a sinusoid (black curve). (c) The sine and cosine amplitudes (red and blue curves) are the whirl's (**W**) imaginary and real complex values, for a given wavenumber. The vertical offset of the fit is the ordinary spectrum (green, B_{ord}) at that wavenumber. Graphics reproduced from Ref. 1. (See electronic edition for a color version of this figure.)

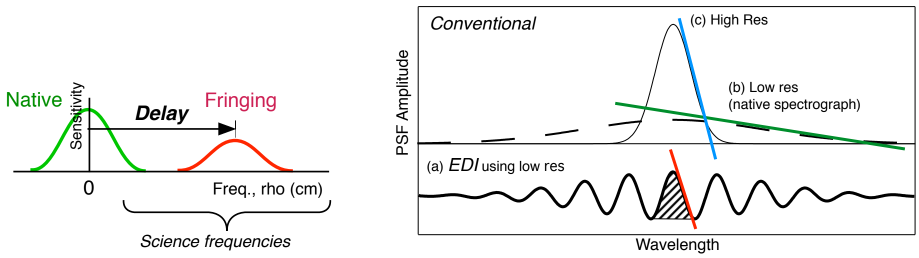

Fig. 10. Two manifestations of the EDI instrument response: left graphic is in frequency space, and right graphic is along dispersion axis (pixel, wavenumber σ, or wavelength $\lambda = 1/\sigma$ space). (Left) Heterodyning shifts the native spectrograph sensitivity peak (green) from zero to a higher frequency (red) where science frequencies typically reside, by delay τ, and an amplitude of 50%. Frequency in units of features per wavenumber (cm^{-1}), conveniently has the same units of delay, units of cm. (Right) The EDI instrument response is a corrugated peak or wavelet (bold curve (a)), which has an inner portion having much higher slope (and thus higher Doppler sensitivity) than the low resolution native spectrograph alone (dashes, (b)), which defines the envelope. The slope of the sinusoid is proportional to τ. For use in high resolution spectroscopy, the central area (cross-hatched) is made unambiguous by combining several wavelets of different periodicities (delays), as demonstrated in Fig. 14. Graphics reproduced from Ref. 16. (See electronic edition for a color version of this figure.)

native spectrograph (b), and an interior sinusoid whose frequency is proportional to delay τ, which can be set by the user to be almost arbitrarily high. Note that the slope (red line) of a fringe inside the wavelet can be much higher than the slope (green) of the native spectrograph — it can easily be as high as the high resolution spectrograph lineshape (c, blue).

3.1.5. *Moiré Phase Yields Doppler Velocity*

The moiré phase shift between two observations is proportional to the Doppler velocity shift of the input source. To make the measurement independent of drifts in τ, such as due to thermal changes in the optical mounts, the moiré patterns of a reference spectrum such as iodine are also simultaneously observed on the same detector. These are separated from the stellar component mathematically. Then the change in the above two velocity shifts yields the corrected Doppler velocity. This is independent to small ($< \lambda/4$) drifts in τ since these affect the stellar and iodine moiré phase by the same amount. For example, the open air EDI shown in Fig. 6, not having thermal or environmental controls, was used to make the few m/s precision Doppler measurements shown in Fig. 11.

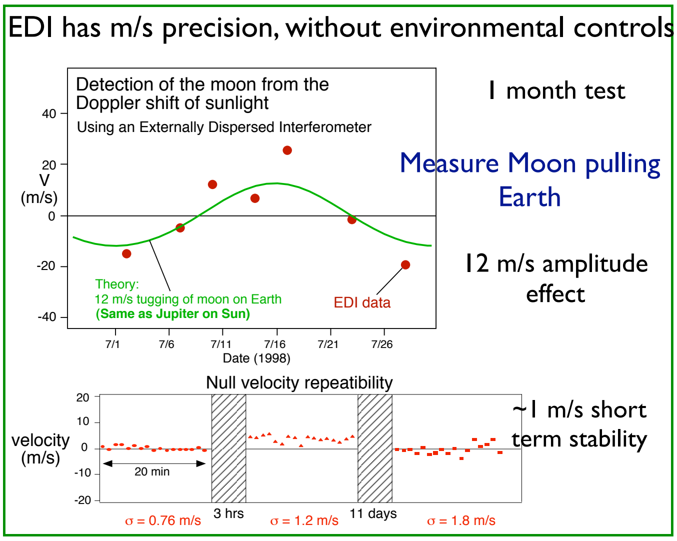

Fig. 11. (Upper) Doppler velocity of sunlight[7] over a month's time detects the 12 m/s amplitude tugging of the Moon on Earth. (Lower) a bromine cell mimics the spectra of a zero velocity source (which then passes through the iodine cell), demonstrating m/s scale repeatability on a 11 day time scale. The EDI shown in Fig. 6 (Ref. 8) was used as depicted (but with an iodine cell at the fiber end) without any environmental thermal or mechanical stabilization. The 20k resolution native spectrograph used without the interferometer would have insufficient resolution and prohibitively large drift of its lineshape to allow such precision. Note that the symbol σ in this figure refers to the standard deviation of the data values, not to wavenumber. (See electronic edition for a color version of this figure.)

3.1.6. *Moiré Shape Yields High Resolution Spectrum*

The same EDI apparatus used for Doppler velocimetry can be used to perform high resolution spectroscopy,[5,16] also referred to as resolution boosting (as in Figs. 14 –

18) by using a different kind of analysis. The moiré patterns are processed mathematically to reverse the heterodyning frequency shift that originally occurred optically. Whereas the original optical heterodyning lowered the frequencies to form the moiré patterns recorded on the detector, a multiplication by $e^{i2\pi\sigma\tau}$ increases the frequency by amount τ, restoring the signal to its original high frequency. After appropriate filtering (called equalization) to reshape the net frequency response into a Gaussian, a reconstructed spectrum is produced having its resolution boosted over the native resolution. (Examples shown in Section 3.3 below.)

3.2. *Demonstrations of EDI Doppler Velocimetry*

3.2.1. *Initial testing on sunlight*

Figure 6 (left) shows a photo of (essentially) the EDI apparatus used to make solar measurements for initial testing of the EDI concept (the iodine cell was not in the beam path in this photo). A fiber from a roof-mounted heliostat brought sunlight to a laboratory optical table on which the interferometer resided. Figure 11 (upper) shows the 12 m/s signature of the Moon tugging the Earth in the measurement of the solar radial velocity over a month's time. Figure 11 (lower) shows the zero-velocity test by measuring *vs.* time the velocity of a bromine absorption cell (which is a faux-star that is, of course, stationary), relative to the iodine cell, which is also stationary. We see only a few m/s drift over 11 days, which is excellent for an unstabilized cavity and environmentally unprotected system.

This is remarkable because no environmental thermal or mechanical stabilization was used (the short exposure times did not require interferometer fringe stabilization), whereas a conventional spectrograph typically requires such environmental control. This is possible because the EDI technique transfers the responsibility of the high resolution measurement from the native spectrograph to the interferometer. The interferometer is more robust to drifts in beam profile because a sinusoidal fringe has only three significant degrees of freedom (phase, magnitude, and intensity offset) whereas the point spread function of a grating spectrograph can have many more degrees (of order one for each diffraction grating groove involved).

3.2.2. *New Exoplanet Detected*

A new exoplanet HD 102195b was discovered[12] by Jian Ge's team using the EDI technique with the ET instrument (Fig. 12) at the moderately small aperture 0.9 m Kitt Peak Nat. Obs. telescope. The small aperture discovery was possible because of the high throughput[11] (49% from fiber output to detector) enabled by the lower native spectrograph resolution (R∼5000) allowed by the EDI technique. This native resolution is too low to perform precision radial velocimetry without the benefit of an interferometer.

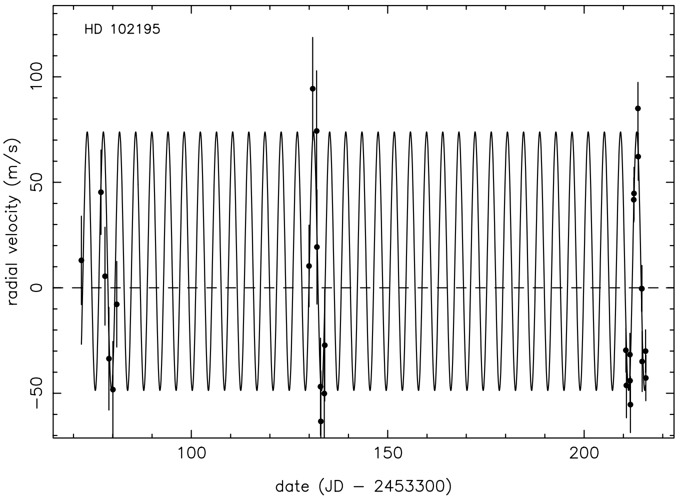

Fig. 12. Discovery[12] of a new exoplanet HD 102195b, performed in spring 2005 by Jian Ge's team using the ET instrument[11] at the Kitt Peak Nat. Obs. (KNPO) 0.9 m coudé feed, and later by ET at the 2.1 m KNPO telescope. Velocity errors are ∼10 and ∼20 m/s for the 2.1 m and coudé feed, respectively. The solid curve is the orbital fit. The native spectrograph has only 5000 resolution, which is too low for precision radial velocimetry without an interferometer. Planetary discovery with a 0.9 m telescope of a V=8.05 magnitude star is possible due to the high throughput of the instrument (49% from fiber output to detector), allowed by the lower native spectrograph resolution requirement of the EDI technique. Graphics reprinted from Ref. 12, Copyright (2006), with permission from AAS.

3.2.3. *Mt. Palomar Hale telescope: Doppler*

An EDI version called "TEDI" was mounted on the mirror of the 5-meter Hale telescope at Mt. Palomar Observatory inside the Cassegrain output hole, in series with the TripleSpec[17] near-infrared echelle spectrograph, of bandwidth 0.95 – 2.45 μm (4100 - 10500 cm^{-1}), to test on M-stars. The native resolution of 2,700 is insufficient by itself to perform precision Doppler velocimetry, and the Cassegrain mounting produced a changing gravity vector which would cause problems for a conventional instrument. Yet Figure 13 shows that accurate radial velocity data on an M-star in the near infrared was obtained over several months. Insufficient calibration of telluric lines was believed to be the dominant error source.

3.3. *Demonstrations of EDI High Resolution Spectroscopy*

The primary purpose of TEDI was to demonstrate Doppler measurements, and eight delays (0.1, 0.3, 0.7, 1, 1.3, 1.7, 2.9, 4.6 cm) were provided to optimize for different rotational linewidths of different stars. However, we realized that the multiple delays also presented an opportunity to demonstrate high resolution spectroscopy with a boost factor much higher than the ∼2x boost demonstrated earlier with a

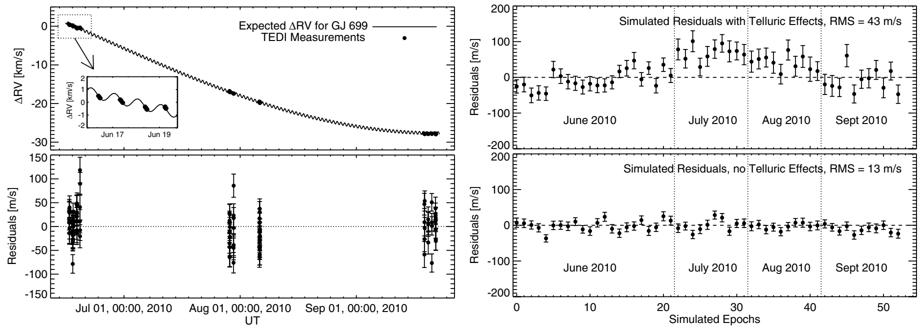

Fig. 13. (Left panels) Radial velocity measurements of star GJ 699 in the near infrared with the TEDI instrument at the Hale telescope. (Upper left) Solid curve shows expected behavior. The data clearly measures the effect of the Earth's motion (30 km/s component from solar orbit, 300 m/s component from rotation) with residuals in bottom left panel. The 2700 native spectrograph resolution is insufficient to perform precision radial velocimetry without the interferometer. The Cassegrain mounting produces a changing gravity vector. Yet the dominant error is believed to be insufficient calibration of telluric lines since removing them in a simulation (bottom right) reduced error from 43 to 13 m/s, which matches the expected photon noise. Graphics reproduced from Ref. 14 with permission from PASP.

single delay EDI.[15] These TEDI high resolution demonstrations (Fig. 14, Fig. 16) were very successful[1,16] and a resolution boost as high as 10x was achieved.

Figure 14(a) shows that with multiple delays the high resolution EDI output spectrum is a sum over many wavelets, one per delay. Figure 14(b) shows that a ThAr doublet can be easily resolved by the EDI, even though this doublet separation is smaller than the native spectrograph resolution element.

Figure 15 shows the instrument response in Fourier space, which is called a Modulation Transfer function (MTF). The peaks demark positions in delay space of the installed glass etalons. A contiguous coverage of delay space is desired to form a net Gaussian response (after equalization removes the dips), otherwise gaps cause ringing in the effective instrument lineshape. For the early data of Figure 14 the largest contiguous range was up to 1.7 cm using E1 - E6, because the gap at 2.4 cm prevented use of E7.

Later data such as Figure 16 was taken with benefit of a new delay E6.5 at 2.4 cm, which filled this gap and extended the contiguous delay range to 2.9 cm. The wider delay range allowed a higher reconstructed resolution in Figure 16, a tenfold boost. Since the "filter" wheel held only eight glass etalons and we installed E6.5 in the E1 position.

An even higher boost of 45,000 could be achieved by including two more delays at 3.5 and 4 cm to fill the gap between E7 and E8 and form a contiguous range up to 4.6 cm. (Supposing we obtain a filter wheel that holds more than eight delays.)

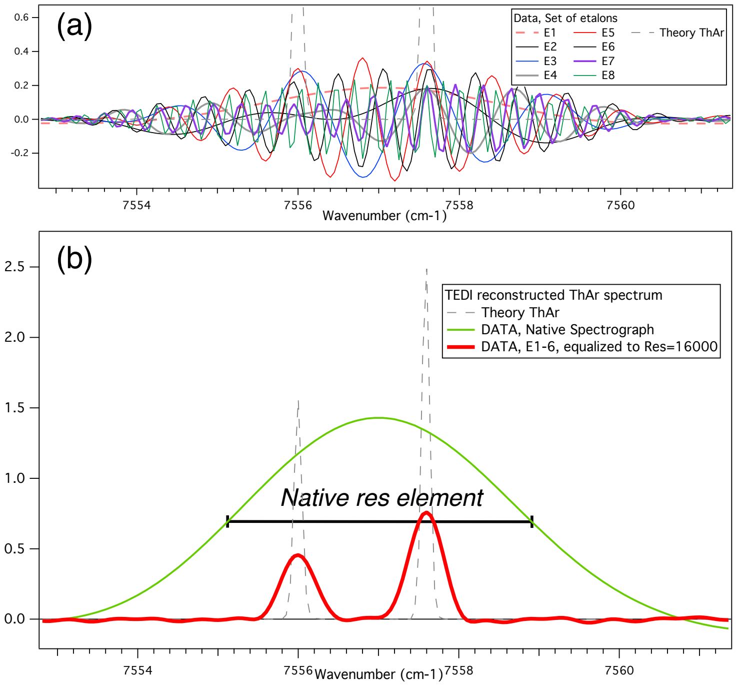

Fig. 14. (a) Reconstruction of an otherwise unresolved ThAr doublet (7556, 7557.6 cm^{-1}) from many wavelets measured at multiple delays. (b) The native spectrograph (green curve) cannot resolve the doublet. The EDI reconstructed spectrum (red curve), which is sum of wavelets, then equalized to $R = 16,000$, easily resolves the doublet. The data were measured by the TEDI interferometer at the Hale 200 inch telescope in series with the TripleSpec NIR spectrograph (0.95 – 2.45 μm), using six delays of 0.1 – 1.7 cm. Graphics reproduced from Ref. 16. (See electronic edition for a color version of this figure.)

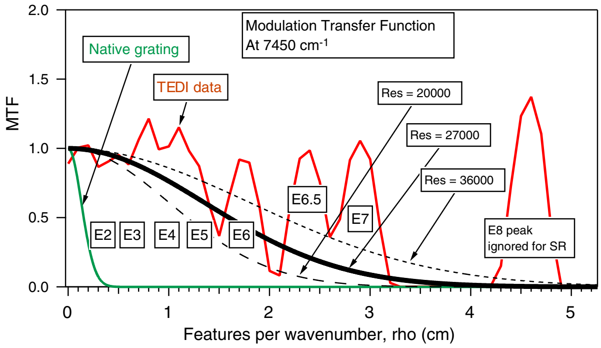

Fig. 15. Modulation Transfer Function (MTF) for the EDI evaluated at wavenumber 7450 cm^{-1} shows instrument sensitivity to a given frequency along the dispersion axis in features per wavenumber, as variable rho, which also has units of delay in cm. The MTF here describes later data, including that of Figure 16, where the gap at 2.4 cm between E6 and E7 was filled by purchase of a new delay E6.5, which was swapped for E1 (our apparatus could only hold eight delays). In this MTF, each delay (E2 - E8, 0.3 - 4.6 cm) produces a peak in sensitivity (red curve), which has the same width as the native spectrograph peak (green curve) positioned at zero, but centered at its delay value. The goal of using multiple delays of different values is to create a net sensitivity curve which has no gaps. Later during analysis, multiplication by an equalization curve removes the dips to create an ideal Gaussian shaped MTF (black dashed curves of various resolution). The wider range of delays allowed a higher reconstructed resolution. The highest delay E8 at 4.6 cm could not be included in spectral reconstruction due to gap between E7 and E8, but was useful for measuring Doppler shifts because it was the most sensitive due to its large delay. Graphics reproduced from Ref. 16. (See electronic edition for a color version of this figure.)

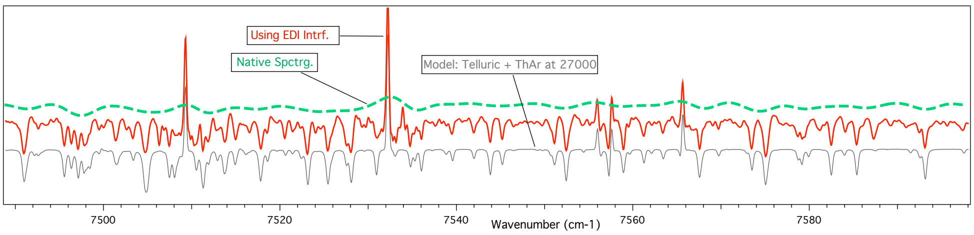

Fig. 16. Demonstration of 10-fold resolution boost observing star κ CrB. The native spectrum (green dashes), with resolution $R = 2,700$, cannot resolve the telluric features. The TEDI spectrum (red curve) used 7 contiguous delays, up to 2.9 cm, to produce resolution 27,000. The model of telluric[18] and ThAr[19] (gray curve) blurred to 27,000 resolution, shows excellent agreement. Resolution boosting occurs simultaneously across the full bandwidth (0.9-2.45 μm) of the native TripleSpec spectrograph, with a resolution changing as (maximum delay/wavelength). Graphic reproduced from Ref. 20. (See electronic edition for a color version of this figure.)

3.4. *Other Advantages of EDI*

3.4.1. *Extremely Wide Bandwidth*

Figure 17 demonstrates the very wide bandwidth of EDI, unlimited by the interferometer component and only limited by the bandwidth of the native spectrograph. In contrast, the conventional method of reducing slitwidth to increase resolution requires increasing the number of detector pixels. (Or if the number of pixels is kept fixed, the bandwidth decreases reciprocally to the resolution increase.) This wide bandwidth is possible because the EDI interferometer comb has a period that is essentially uniform across the band (only slightly changing with glass dispersion). Figure 21 of Sect. 4 compares interferometer combs of EDI with the strongly wavenumber dependent comb of SHS.

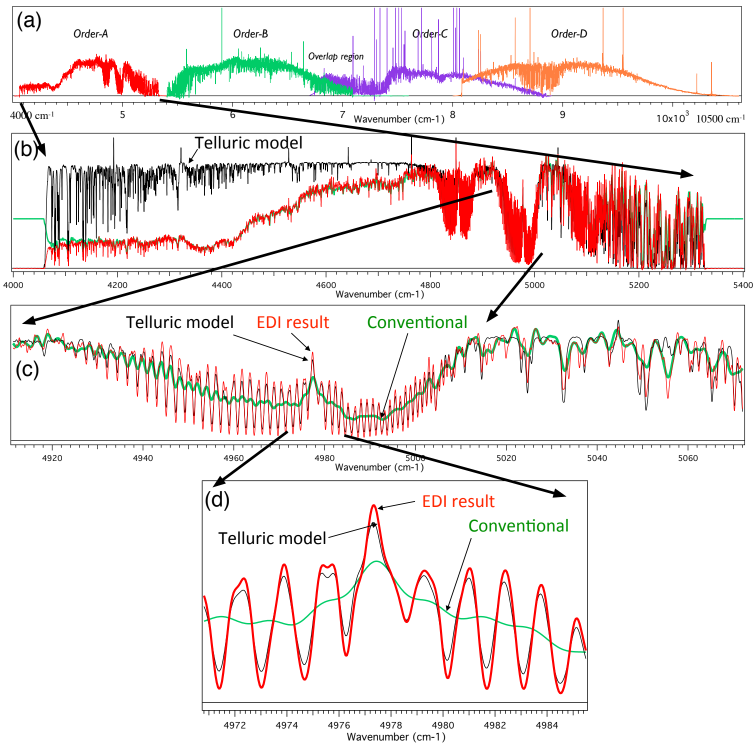

Fig. 17. An externally dispersed interferometer has an extremely wide bandwidth limited only by the native spectrograph, because the sinusoidal comb of the external interferometer has a uniform period, not dependent on the angle of diffraction from an internal grating. (a) This TEDI reconstructed spectrum spans 4 orders of the TripleSpec echelle spectrograph in the NIR (4100-10500 cm^{-1}), observing HD219134 at resolution $R = 11,000$ (4x boost). Panels (b,c,d) zoom in telluric feature near $\sim$4980 cm^{-1} due to CO_2 molecule. Graphics reproduced from Ref. 16. (See electronic edition for a color version of this figure.)

3.4.2. *Immunity to Additive Fixed-Pattern Noise*

Because data are collected in multiple exposures in a phase-stepping manner, only fringes that vary synchronously to the commanded interferometer phase increment appear in the processed moiré signal. Hence EDI is immune to additive offsets or fixed-pattern errors that often plague the ordinary spectrum. In TEDI such fixed-pattern errors were due to bad pixels and background emissions. Figure 18 of the ThAr lamp, at 9174 and 9214 cm^{-1}, are examples of how the EDI signal (red curve) is immune to bad pixels that pollute the native spectrum (green curve).

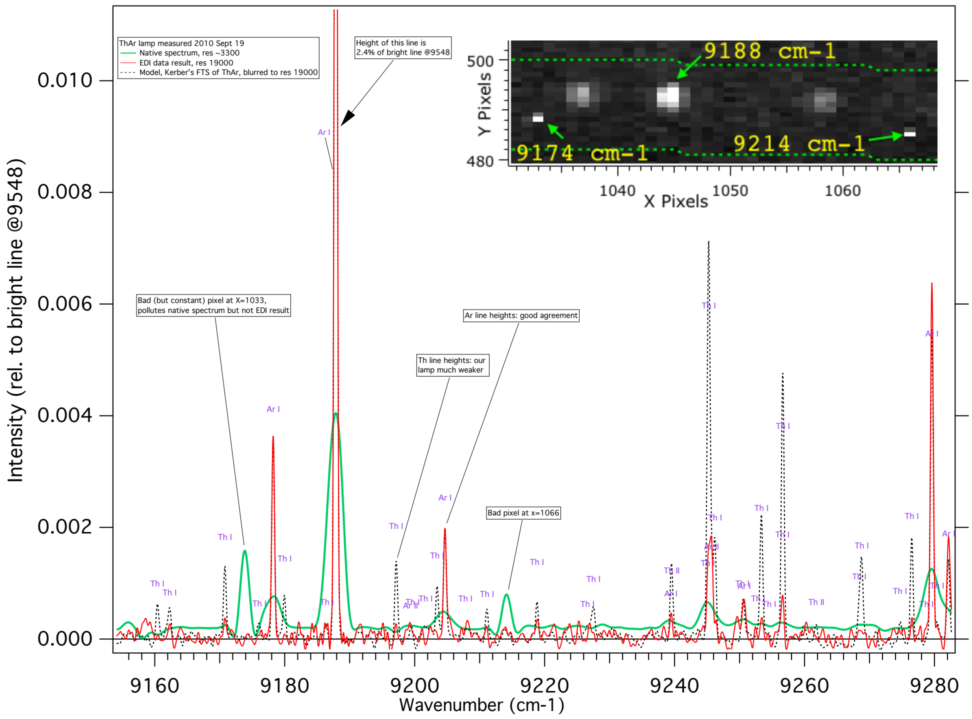

Fig. 18. Measurement (red curve) of TEDI's ThAr lamp to a 6x boosted resolution of 19,000, compared to a National Institute of Standards and Technology (NIST) measurement[19] of a different ThAr lamp blurred to the same resolution (black dashes), D-order. Purple text is the NIST assignment of species. The native spectrograph (green curve) has a resolution of ∼3300. The lower heights of Th lines relative to Ar lines for our lamp are consistent (Fig. 7 of Ref. 22) with the smaller current (∼10 mA) we used *vs.* that used by NIST (∼20 mA). Note the extremely high dynamic range of the measurement — ∼0.1% lines are easily observed (heights are fraction of 9548 cm^{-1} line). The EDI curve is robust to fixed-pattern noise such as false peaks in the native spectrum at 9174 and 9214 cm^{-1} due to bad pixels at X=1033 and 1066 (inset shows detector there). Bad pixels are constant and thus do not affect whirls, which look at changes between exposures. Graphics reproduced from Ref. 16. (See electronic edition for a color version of this figure.)

3.4.3. *Robustness to Wavelength Drift of Native Spectrograph*

Besides boosting the resolution of a spectrograph beyond the limits imposed by classical optics (slitwidth, focal blur, detector pixel spacing etc.), the other important advantage of EDI is that it is extremely robust to errors in the native spectrograph point spread function shape and position. Figure 19 (top) shows severe and irregular wavelength drifts suffered by the TEDI native spectrograph while observing starlight. Yet we still obtained high resolution spectra under these drifts.

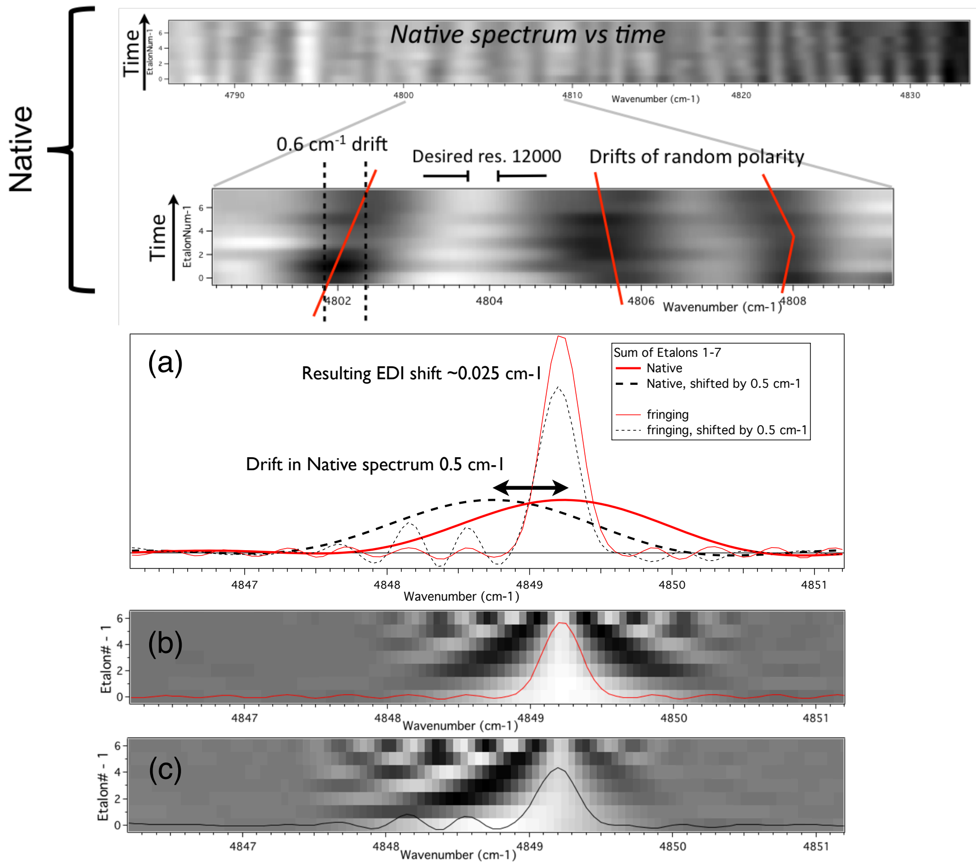

Fig. 19. Top panel: Large and irregular PSF drifts in the native spectrograph, to which EDI is robust. Rows are native spectra *vs.* etalon #, and hence versus time (∼10 minutes apart). Lower three panels: Calculated EDI reaction to a native spectrograph PSF translation using actual ThAr moiré data and processing pipeline, but translating every input by 0.5 cm^{-1} to the left. (a) Red and black curves are unshifted and shifted output spectra respectively, formed from sums over (b) unshifted, and (c) shifted wavelet stacks. The spectrograph drifts largely only affect the envelope of the wavelets, rather than the phase, and the phase is most critical for determining the peak location. The peak centroid shifts 0.025 cm^{-1}, hence a factor 20x reduction. A further reduction of an order magnitude or more can be obtained by strategically shaping the instrument response.[21] Graphics reproduced from Ref. 16. (See electronic edition for a color version of this figure.)

Figure 19 (bottom 3 panels) is a simulation using TEDI data of a ThAr line that is deliberately shifted across the detector, to show that the output spectra reacts by only a small shift, 1/20th of the applied shift. A further reduction of an order of magnitude or more can be obtained by strategically shaping the instrument response so that a cross-fading occurs between overlapped lineshapes of neighboring delays.[21] A numerical simulation in Sect. 10 of Ref. 16 shows a reaction 350x smaller than the applied wavenumber shift.

The robustness of EDI to native spectrograph lineshape distortions and drift is an important practical advantage, since such distortions often form the limiting floor to the achievable radial velocity noise.

4. Spatial Heterodyning Spectroscopy (SHS, HHS)

Internally dispersed interferometers such as spatial heterodyning spectroscopy[23–29] (SHS) and the similar heterodyned holographic spectroscopy[30] (HHS) have the great practical advantage of not requiring any moving parts to measure a spectrum. Instead of sampling delay space *vs.* time by scanning a delay, they splay delay space spatially across an integrating detector and measure the many delay values at once simultaneously, as depicted in Fig. 1(d).

Figure 20(a) is a schematic of a basic SHS apparatus,[24,30] and (b) shows the formation of sinusoidal fringes whose spatial frequency is proportional to the distance $\delta\sigma = \sigma - \sigma_0$ of a wavenumber σ from a base value wavenumber σ_0 which is set by the Littrow angle of the gratings (which is when a diffracted beam retroreflects). The gratings at the end of each interferometer arm are configured to retroreflect light at wavenumber σ_0, and for these wavenumbers the wavefronts from the two arms are aligned parallel and hence produce a fringe that has a uniform intensity across the detector.

For other wavenumbers, the diffraction from the gratings causes the beams arriving at the beamsplitter to have an angle different than σ_0, creating a sinusoidal fringe pattern. This angle increases with $\delta\sigma$. Hence the spatial frequency of the fringe across the detector is proportional to $\delta\sigma$. A Fourier transform is then applied to the interferogram to convert it into wavenumber-space, one that is offset from σ_0. Effectively the SHS creates many pathlength differences that are detected simultaneously. Hence in the zoology of instrument types shown in Fig. 1, in (d) we notionally show the SHS by a rectangle, to suggest the many delay values being sensed simultaneously.

Figure 21 compares how EDI (middle) and SHS or HHS (lower) interact with a simulated absorption spectra having a continuum. This is useful for comparison, even if there is actually no external cross-dispersion along the horizontal for the SHS in panel (c). (In that case, one mentally collapses the horizontal axis of (c).) In some versions of SHS,[25] an external cross-disperser is used.

The key point is that for a single narrow spectral feature in the SHS, which makes

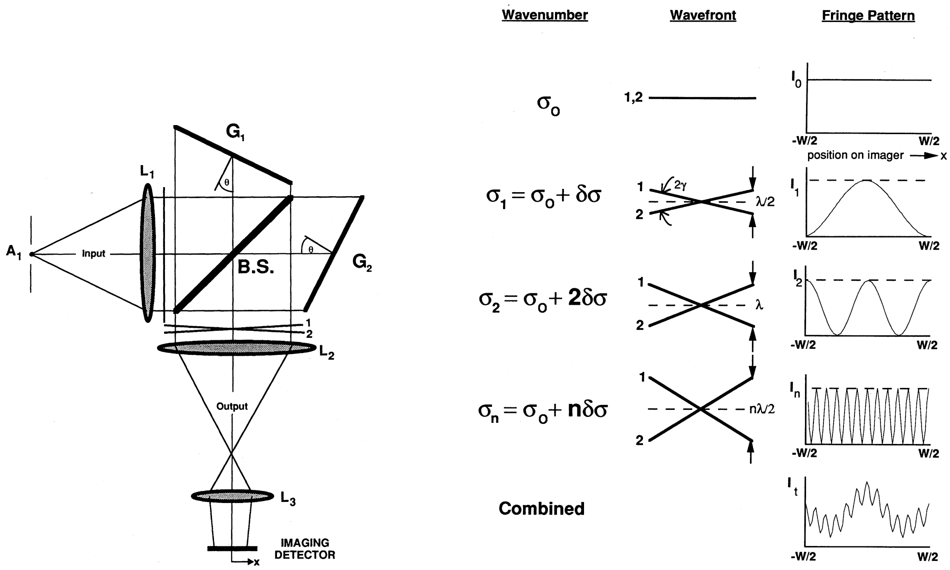

Fig. 20. (Left) Schematic of a basic Spatial Heterodyning Spectrometer (SHS). The single initial wavefront, shown as a vertical line just to the right of lens L_1, is converted by the gratings G_1 and G_2 into two tilted wavefronts (labeled 1 and 2 just before lens L_2), where the tilt angle depends on the wavenumber, as shown in the right-hand panel. (Right) Explanation of how different wavenumbers σ will intersect at different angles for the two interferometer arms, due to the gratings at the end of each arm which disperse the light. This causes the sinusoidal fringe pattern at the detector to have different spatial frequencies, proportional to the change $\delta\sigma = \sigma - \sigma_0$ in wavenumber from σ_0. The base wavenumber, σ_0, is the wavenumber at which the wavefronts combine parallel to each other, being retroreflected from the grating at the Littrow condition for this wavenumber. Since the detected pattern spatial frequency is proportional to $\delta\sigma$, and since multiple spatial frequencies corresponding to different wavenumber features can be recorded simultaneously, in an additive fashion, then taking the Fourier transform of the detected fringe pattern reveals the distribution of $\delta\sigma$ in the source spectrum. Graphics reprinted from Ref. 24, Copyright (1992), with permission from AAS.

a vertical line, a sinusoidal pattern is made that has a vertical spatial frequency that increases linearly with distance $\delta\sigma = \sigma - \sigma_0$ from the center of the diamond-like structure at σ_0. Hence the vertical period is reciprocally related to σ_0 and it creates the diamond-like shape. For the range σ which are close to σ_0 the spectral resolution can be extremely high.

However, for large $\delta\sigma$ the spatial frequency can eventually increase to beyond the Nyquist frequency in the vertical that the finite detector pixel spacing can resolve. This sets the edge of the bandwidth for the SHS. However, in some versions of SHS the use of an echelle grating[24] creates different diffraction orders that are separately detected and have separate bandwidth average positions. This allows the aggregate bandwidth to be larger.

The photon noise for absorption spectroscopy (which has a continuum background to contribute noise from other wavenumbers) is worse than a dispersive

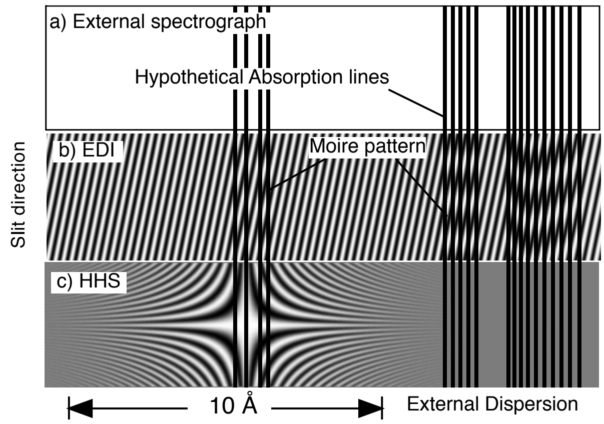

Fig. 21. A graphic useful for considering the behavioral difference between the externally dispersed (b, EDI) and a basic internally dispersed behaviors (c, SHS or HHS), even if there is actually no external cross-dispersion in panel (c). (One can mentally sum all the external dispersion channels together.) For the hypothetical absorption lines (a), the EDI (b) has an essentially uniform period across the whole band, while the SHS has a period that varies reciprocally with $\delta\sigma = \sigma - \sigma_0$, creating a diamond-like shape at σ_0. This depicts absorption spectroscopy where there is a continuum to illuminate the bulk of the comb, rather than emission spectroscopy with a dark background. Graphic reprinted from Ref. 7, Copyright (2003), with permission from PASP.

spectrograph by the square root of number of overlapping signals that fall on the same detector pixel (Eq. A40 of Ref. 30). By the Nyquist theorem, the number of distinct spatial frequencies that can be resolved by a row of pixels could be as much as half the pixels along the delay dimension.

Figure 22 (left) shows an interferogram of a Hg source. The spatial frequency of each column yields the wavenumber of the associated Hg line. Figure 22 (right) shows the spectra obtained by Fourier transform of the interferogram columns.

Figure 23 shows a monolithic SHS interferometer for the Doppler asymmetric spatial heterodyne (DASH) project,[27,28] which measures atmospheric wind velocities. The triangular edges of the Koster's prism beamsplitter are 100 mm long. Figure 24 shows a comparison of the SHS (DASH) wind velocities to the more conventional Fabry-Perot interferometer (FPI) instrument results, both measuring winds from the ground on the same night. The dashed line represents zero wind velocity. The HWM07 is a Horizontal Wind Model based on historical data.

Because SHS (and EDI) do not have moving optical parts to scan a delay, they can employ additional optical elements to dramatically increase their etendue (product of beam area times solid angle), called field-widening, which makes their spectral properties independent of the entering beam angle for a wider range of angles. Conventional dispersive spectrographs typically do not employ field widening, so their etendue is much smaller. This makes the SHS particularly well suited for measuring extended diffuse sources, such as air glow and atmospheric winds (Figs. 23 and 24).

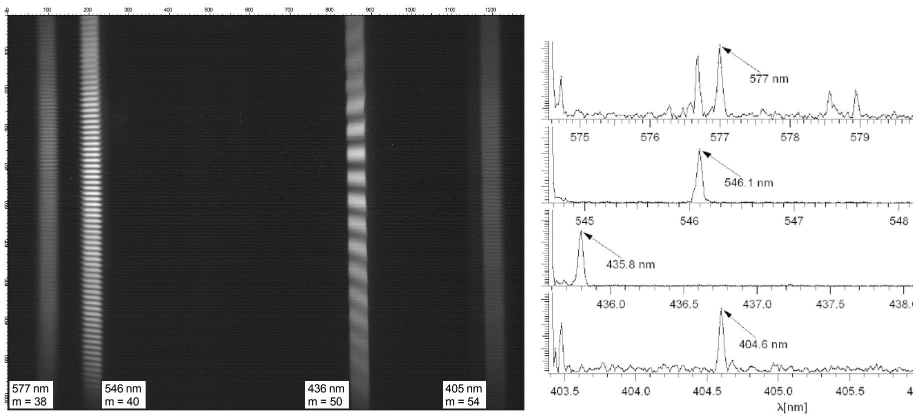

Fig. 22. (Left) Interferogram data of a Hg source. The spatial frequency of each column yields the wavenumber of the associated Hg line. (Right) Spectra obtained by Fourier transform of the interferogram columns. Graphics reproduced from Ref. 25 with permission from SPIE and author.

Fig. 23. Monolithic field-widened SHS interferometer for the DASH project that measures atmospheric wind velocities. The triangular edges of the Koster's prism beamsplitter are 100 mm long. Photo reprinted from Ref. 27, Copyright (2010), with permission from OSA.

In field-widening, an element such as an etalon, prism, or lens is added to superimpose the virtual or real image of the grating or end mirror of one arm of the interferometer onto the grating or end mirror of the other arm. Therefore it appears, according to ray angle, that the interferometer has zero delay. But in reality, by time-of-flight of a hypothetical pulse of light there is a nonzero delay between the arms due to the slower speed of light through glass and a related positional offset. The time of flight difference between the arms accomplishes the desired interferometric spectral behavior, while acting as a zero delay device regarding beam angle. A zero delay interferometer has zero delay for all angles. Hence the field-widened interferometer imposes the same nonzero time delay for all rays, independent of ray angle (except where the small angle approximation of Snell's law breaks down).

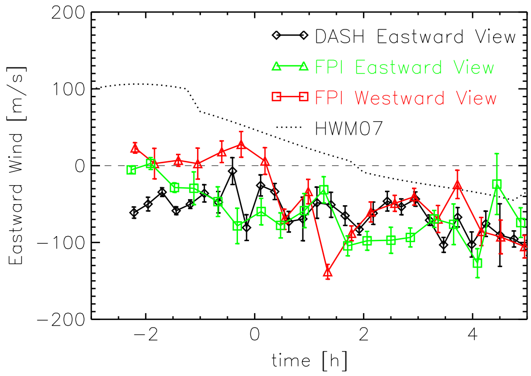

Fig. 24. Comparison of the SHS (DASH) wind velocities to the more conventional Fabry-Perot interferometer (FPI) instrument results, both measuring winds from the ground on the same night. The dashed line represent zero wind velocity. The HWM07 is a Horizontal Wind Model based on historical data. Photo reprinted from Ref. 28, Copyright (2012), with permission from Elsevier. (See electronic edition for a color version of this figure.)

Acknowledgments

This material is based upon work supported by the National Science Foundation under Grant No. AST-0505366, AST-096064, PAARE AST-1059158, NASA Grant NNX09AB38G, and by Lawrence Livermore Nat. Lab. under Contract DE-AC52-07NA27344.

References

1. D. J. Erskine, J. Edelstein, E. Wishnow, M. Sirk, P. S. Muirhead, M. W. Muterspaugh, and J. P. Lloyd, High-resolution broadband spectroscopy using externally dispersed interferometry at the Hale telescope: part 2, photon noise theory, *J. Astron. Tele. Instr. Sys.* **2**(4), 045001, (2016). ISSN 2329-4124. doi: 10.1117/1.jatis.2.4.045001. URL `http://dx.doi.org/10.1117/1.JATIS.2.4.045001`.
2. A. R. Hajian, B. B. Behr, A. T. Cenko, R. P. Olling, D. Mozurkewich, J. T. Armstrong, B. Pohl, S. Petrossian, K. H. Knuth, R. B. Hindsley, M. Murison, M. Efroimsky, R. Dantowitz, M. Kozubal, D. G. Currie, T. E. Nordgren, C. Tycner, and R. S. McMillan, Initial Results from the USNO Dispersed Fourier Transform Spectrograph, *ApJ.* **661**, 616–633, (2007). doi: 10.1086/513181.
3. B. B. Behr, A. R. Hajian, A. T. Cenko, M. Murison, R. S. McMillan, R. Hindsley, and J. Meade, Stellar astrophysics with a dispersed Fourier transform spectrograph.

I. Instrument description and orbits of single-lined spectroscopic binaries, *ApJ.* **705**, 543–553, (2009). doi: 10.1088/0004-637X/705/1/543.

4. B. B. Behr, A. T. Cenko, A. R. Hajian, R. S. McMillan, M. Murison, J. Meade, and R. Hindsley, Stellar Astrophysics with a Dispersed Fourier Transform Spectrograph. II. Orbits of Double-lined Spectroscopic Binaries, *AJ.* 142:6 (July, 2011). doi: 10.1088/0004-6256/142/1/6.
5. D. J. Erskine and J. Edelstein. Interferometric resolution boosting for spectrographs. In eds. A. Moorwood and M. Iye, *Ground-based Instrumentation for Astronomy*, vol. 5492, *Proc. SPIE*, pp. 190–199, (2004). doi: 10.1117/12.549947.
6. J. Edelstein and D. J. Erskine. High Resolution Absorption Spectroscopy using Externally Dispersed Interferometry. In *UV, X-ray & Gamma Ray Astr. Space Instrm.*, vol. 5898, *Proc. SPIE*, (2005).
7. D. J. Erskine, An externally dispersed interferometer prototype for sensitive radial velocimetry: theory and demonstration on sunlight, *PASP.* **115**, 255–269, (2003).
8. D. J. Erskine and J. Ge. Novel Interferometer Spectrometer for Sensitive Stellar Radial Velocimetry. In eds. W. van Breugel and J. Bland-Hawthorn, *Imaging the Universe in Three Dimensions: Astrphys. Advncd. Multi-Wavel. Imaging Devices*, vol. 195, *ASP Conf. Series*, pp. 501–507, (2000). URL `http://digital.library.unt.edu/ark:/67531/metadc780974/`.
9. D. J. Erskine, Combined dispersive/interference spectroscopy for producing a vector spectrum, *US Patent.* **6,351,307** (Issued Feb. 26,, 2002).
10. J. Ge, D. J. Erskine, and M. Rushford, An externally dispersed interferometer for sensitive Doppler extra-solar planet searches, *PASP.* **114**, 1016–1028, (2002).
11. J. Ge, S. Mahadevan, J. C. van Eyken, C. DeWitt, J. Friedman, and D. Ren. All-sky extrasolar planet searches with multi-object dispersed fixed-delay interferometer in optical and near IR. In *Ground-based Instrumentation for Astronomy. Edited by Alan F. M. Moorwood and Iye Masanori. Proceedings of the SPIE, Volume 5492, pp. 711-718 (2004).*, vol. 5492, pp. 711–718, (2004). doi: 10.1117/12.551989.
12. J. Ge, J. van Eyken, S. Mahadevan, C. DeWitt, S. R. Kane, R. Cohen, A. Vanden Heuvel, S. W. Fleming, P. Guo, G. W. Henry, D. P. Schneider, L. W. Ramsey, R. A. Wittenmyer, M. Endl, W. D. Cochran, E. B. Ford, E. L. Martín, G. Israelian, J. Valenti, and D. Montes, The first extrasolar planet discovered with a new-generation high-throughput Doppler instrument, *ApJ.* **648**, 683–695, (2006). doi: 10.1086/505699.
13. J. C. van Eyken, J. Ge, and S. Mahadevan, Theory of Dispersed Fixed-delay Interferometry for Radial Velocity Exoplanet Searches, *ApJS.* **189**, 156–180, (2010). doi: 10.1088/0067-0049/189/1/156.
14. P. S. Muirhead, J. Edelstein, D. J. Erskine, J. T. Wright, M. W. Muterspaugh, K. R. Covey, E. H. Wishnow, K. Hamren, P. Andelson, D. Kimber, T. Mercer, S. P. Halverson, A. Vanderburg, D. Mondo, A. Czeszumska, and J. P. Lloyd, Precise stellar radial velocities of an M dwarf with a Michelson interferometer and a medium-resolution near-infrared spectrograph, *PASP.* **123**(904), 709–724, (2011).
15. D. J. Erskine, J. Edelstein, M. Feuerstein, and B. Welsh, High resolution broadband spectroscopy using an externally dispersed interferometer, *ApJ.* **592**, L103–L106, (2003).
16. D. J. Erskine, J. Edelstein, E. H. Wishnow, M. Sirk, P. S. Muirhead, M. W. Muterspaugh, J. P. Lloyd, Y. Ishikawa, E. A. McDonald, W. V. Shourt, and A. M. Vanderburg, High-resolution broadband spectroscopy using externally dispersed interferometry at the Hale telescope: part 1, data analysis and results, *J. Astron. Tele. Instr. Sys.* **2**(2), 025004, (2016). doi: 10.1117/1.JATIS.2.2.025004. URL `http:`

//dx.doi.org/10.1117/1.JATIS.2.2.025004.

17. J. C. Wilson, C. P. Henderson, T. L. Herter, K. Matthews, M. F. Skrutskie, J. D. Adams, D.-S. Moon, R. Smith, N. Gautier, M. Ressler, B. T. Soifer, S. Lin, J. Howard, J. LaMarr, T. M. Stolberg, and J. Zink. Mass producing an efficient NIR spectrograph. In eds. A. Moorwood and M. Iye, *Ground-based Instrumentation for Astronomy*, vol. 5492, *Proc. SPIE*, pp. 1295–1305, (2004). doi: 10.1117/12.550925.
18. H. G. Roe, Titan's atmosphere at high resolution, *Publications of the Astronomical Society of the Pacific*. **115**(812), 1262, (2003). URL http://stacks.iop.org/1538-3873/115/i=812/a=1262.
19. F. Kerber, G. Nave, and C. J. Sansonetti, The Spectrum of Th-Ar Hollow Cathode Lamps in the 691-5804 nm region: Establishing Wavelength Standards for the Calibration of Infrared Spectrographs, *ApJS*. **178**, 374–381, (2008). doi: 10.1086/590111.
20. D. J. Erskine, J. Edelstein, P. Muirhead, M. Muterspaugh, K. Covey, D. Mondo, A. Vanderburg, P. Andelson, D. Kimber, M. Sirk, and J. Lloyd. Ten-fold spectral resolution boosting using TEDI at the Mt. Palomar NIR Triplespec spectrograph. In ed. L. Tsakalakos, *UV/Optical/IR Space Telescopes and Instruments: Innovative Technologies and Concepts V*, vol. 8146, *Proc. SPIE*, (2011). doi: 10.1117/12.892664.
21. D. J. Erskine, E. Linder, E. Wishnow, J. Edelstein, M. Sirk, P. Muirhead, J. Lloyd, and A. Kim. Dramatic robustness of a multiple delay dispersed interferometer to spectrograph errors: how mixing delays reduces or cancels wavelength drift. In *Ground-based and Airborne Instrumentation VI*, vol. 9908, *Proc. SPIE*, p. 99085Y, (2016). doi: 10.1117/12.2230182.
22. F. Kerber, G. Nave, C. J. Sansonetti, P. Bristow, and M. R. Rosa. The spectrum of Th-Ar hollow cathode lamps in the 900-4500 nm region: establishing wavelength standards for the calibration of VLT spectrographs. In ed. C. Sterken, *The Future of Photometric, Spectrophotometric and Polarimetric Standardization*, vol. 364, *ASP Conf. Series*, pp. 461–478, San Francisco, (2007).
23. T. Dohi and T. Suzuki, Attainment of high resolution holographic fourier transform spectroscopy, *Appl. Opt.* **10**(5), 1137–1140, (1971). doi: 10.1364/AO.10.001137. URL http://ao.osa.org/abstract.cfm?URI=ao-10-5-1137.
24. J. Harlander, R. Reynolds, and F. Roesler, Spatial Heterodyne Spectroscopy for the Exploration of Diffuse Interstellar Emission Lines at Far-ultraviolet Wavelengths, *ApJ*. **396**, 730, (1992).
25. A. I. Sheinis, E. Mierkiewicz, F. Roesler, J. Harlander, and A. Bodkin. A spatial heterodyne spectrometer for diffuse H-α spectroscopy. In *Ground-based and Airborne Instrumentation for Astronomy II*, vol. 7014, *Proc. SPIE*, p. 70140I, (2008). doi: 10.1117/12.788470.
26. S. Hosseini and W. Harris. First calibration and visible wavelength observations of Khayyam, a tunable spatial heterodyne spectroscopy (SHS). In *Ground-based and Airborne Instrumentation for Astronomy V*, vol. 9147, *Proc. SPIE*, p. 91478L, (2014). doi: 10.1117/12.2055862.
27. J. M. Harlander, C. R. Englert, D. D. Babcock, and F. L. Roesler, Design and laboratory tests of a doppler asymmetric spatial heterodyne (dash) interferometer for upper atmospheric wind and temperature observations, *Opt. Express*. **18**(25), 26430–26440, (2010). doi: 10.1364/OE.18.026430. URL http://www.opticsexpress.org/abstract.cfm?URI=oe-18-25-26430.
28. C. R. Englert, J. M. Harlander, C. M. Brown, J. W. Meriwether, J. J. Makela, M. Castelaz, J. T. Emmert, D. P. Drob, and K. D. Marr, Coincident thermospheric wind measurements using ground-based Doppler Asymmetric Spatial Heterodyne (DASH) and Fabry-Perot Interferometer (FPI) instruments, *Journal of Atmospheric*

and Solar-Terrestrial Physics. **86**, 92–98, (2012). doi: 10.1016/j.jastp.2012.07.002.

29. A. Bodkin and A. Sheinis. Multiband spatial heterodyne spectrometer and associated methods (Apr. 10, 2012). URL `https://www.google.com/patents/US8154732`. US Patent 8,154,732.
30. N. Douglas, Heterodyned Holographic Spectroscopy, *PASP*. **109**, 151, (1997).